Orbital variations as a major driver of climate and biome distribution during the greenhouse to icehouse transition

Delphine Tardif, Agathe Toumoulin, Frédéric Fluteau, Yannick Donnadieu, Guillaume Le Hir, Natasha Barbolini, Alexis Licht, Jean-Baptiste Ladant, Pierre Sepulchre, Nicolas Viovy, et al.

To cite this version:

Delphine Tardif, Agathe Toumoulin, Frédéric Fluteau, Yannick Donnadieu, Guillaume Le Hir, et al.. Orbital variations as a major driver of climate and biome distribution during the greenhouse to icehouse transition. Science Advances , 2021, 7 (43), ⟨10.1126/sciadv.abh2819⟩. ⟨insu-03401267⟩

HAL Id: insu-03401267
https://insu.hal.science/insu-03401267v1

Submitted on 25 Oct 2021

CLIMATOLOGY

Orbital variations as a major driver of climate and biome distribution during the greenhouse to icehouse transition

Delphine Tardif[1,2]*, Agathe Toumoulin[1], Frédéric Fluteau[2], Yannick Donnadieu[1], Guillaume Le Hir[2], Natasha Barbolini[3], Alexis Licht[1], Jean-Baptiste Ladant[4], Pierre Sepulchre[4], Nicolas Viovy[4], Carina Hoorn[5], Guillaume Dupont-Nivet[6,7]

Recent studies suggest increasing sensitivity to orbital variations across the Eocene-Oligocene greenhouse to icehouse climate transition. However, climate simulations and paleoenvironmental studies mostly provide snapshots of the past climate, therefore overlooking the role of this short-term variability in driving major environmental changes and possibly biasing model-data comparisons. We address this problem by performing numerical simulations describing the end-members of eccentricity, obliquity, and precession. The orbitally induced biome variability obtained in our simulations allows to reconcile previous apparent mismatch between models and paleobotanical compilations. We show that precession-driven intermittent monsoon-like climate may have taken place during the Eocene, resulting in biomes shifting from shrubland to tropical forest in the intertropical convergence zone migration region. Our Oligocene simulations suggest that, along with decreased $p\mathrm{CO_2}$, orbital variations crucially modulated major faunal dispersal events around the EOT such as the Grande Coupure by creating and fragmenting the biome corridors along several key land bridges.

INTRODUCTION

Recently, the application of statistical analysis on the Cenozoic δ^{13}C and δ^{18}O benthic records (*1*) has highlighted an increased climate sensitivity to orbital variations across the late Eocene to early Oligocene. However, numerical simulations are usually performed using a modern orbital configuration and the simulated climate is often described as representative of the studied period, regardless of orbital changes. This approach is problematic because contrasted orbital configurations can lead to profoundly different climates over short periods of time (*2*–*5*). Several modeling studies have demonstrated the impact of orbital variations on some key Eocene greenhouse climatic features. Configurations triggering warm boreal and cool austral summers were shown to favor ice-sheet buildup over Antarctica in the late Eocene (*6*) and to induce seasonal temperature changes by up to 10°C (*3*). They also reinforce the Asian and African monsoons (*7*, *8*) and shrink arid zones to the benefit of more forested biomes due to amplified intertropical convergence zone (ITCZ) migration inland (*9*). The number of modeling studies assessing the sensitivity of the early Oligocene climate to orbital forcing, on the other hand, remains limited apart from studies focusing specifically on the Antarctic glaciation (*6*, *10*, *11*).

The validation of this greenhouse to icehouse climate sensitivity to astronomical forcing is made possible in rare deposits recording and identifying orbital variations over the continents. In eastern China [Jianghan Basin, 42 million years ago (Ma) to 32 Ma], eccentricity-paced evaporite and mudstone deposits suggest oscillations from wetter to drier climates due to monsoon strength variations (*12*). In northeastern Tibet (Xining Basin, 40 Ma to 34 Ma), ephemeral lacustrine deposits record a strong obliquity signal, interpreted as the possible remote forcing exerted by incipient ice sheets on continental Chinese climate (*13*, *14*). In northwestern Europe (Isle of Wight, 35 Ma to 33 Ma), the analysis of clay mineral distribution suggests an eccentricity imprint on the local hydrological cycle (*15*). Orbital forcing imprint is also suggested in Montana (*16*) and in the Ebro Basin in Spain (*17*, *18*).

In addition to these sparse high-resolution records, our understanding of the greenhouse-icehouse transition continental climatic evolution comes mainly from fossilized paleobotanical remains, which offer snapshots of the climate prevailing when they were deposited. Like most pre-Quaternary paleoclimatic indicators, many of these proxies are loosely constrained in space and time and are therefore often implicitly interpreted as reflecting the "average" climate over long periods. The great heterogeneity observed among the various continental archives is apparent from the different compilations of paleoclimatic indicators available for these periods [see (*19*, *20*) and references therein for localities cited below]. While some fieldwork reveals little change in flora throughout the Eocene-Oligocene, as in Patagonia or southeastern and central Europe, on the contrary, other paleosoils and/or paleobotanical studies denote important climatic and floristic shifts toward cooler and drier conditions. Among these, numerous sites indicate that these changes initiated during the late Eocene, for example, in North America, western Europe, and eastern Asia (*20*). Only a few sites, principally in North America and Eurasia, display a change specifically across the eocene-oligocene transition (EOT).

In addition, notable faunal turnover episodes showing a partial replacement of Mongolian, European, and American local mammal

---

[1] Aix Marseille Université, CNRS, IRD, INRA, Collège de France, CEREGE, Aix-en-Provence, France. [2] Université de Paris, Institut de physique du globe de Paris, CNRS, F-75005 Paris, France. [3] Department of Ecology, Environment and Plant Sciences and Bolin Centre for Climate Research, Stockholm University, SE-106 91 Stockholm, Sweden. [4] Laboratoire des Sciences du Climat et de l'Environnement, LSCE/IPSL, CEA-CNRS-UVSQ, Université Paris-Saclay, 91191 Gif-sur-Yvette, France. [5] Department of Ecosystem and Landscape Dynamics, Institute for Biodiversity and Ecosystem Dynamics, University of Amsterdam, Amsterdam 1098 XH, Netherlands. [6] Géosciences Rennes, UMR CNRS 6118, Université de Rennes, Rennes, France. [7] Institute of Geosciences, Potsdam University, Potsdam, Germany.
*Corresponding author. Email: delphine.tardif@hotmail.fr

communities by eastern Asian rodents and lagomorphs are reported through the greenhouse-icehouse. The Mongolian Remodeling (*21–24*) is dated at ca. 34.9 Ma, and the European (*25–27*) and American Grande Coupure are dated around the EOT (33.9 Ma) (*28*) or at the Oi-1 (33.5 Ma) (*25*, *26*), with a possible early migration wave to southeastern Europe in the late Eocene (40 Ma to 35 Ma) (*27*). These pulses in faunal migration, radiating from Asia to other continents, are thought to be the result from a complex interplay between the proto-Tibetan orography evolution (*29*, *30*) and the global cooling and aridification of Asia induced by the combined $p\mathrm{CO_2}$ (partial pressure of $\mathrm{CO_2}$) drawdown and the retreat of the Paratethys Sea initiated at ~40 Ma (*24*, *26*). However, although biome connectivity is an important driver of faunal dispersal (*31*, *32*), the possible influence of orbital cycles on the climate and vegetation coverage of these key land bridges has never been assessed, nor suggested as a potential forcing.

We propose that orbital forcing may have played a substantial part in explaining the substantially heterogeneous history of biome reconstruction throughout the late Eocene period. To this end, we simulate late Eocene climate and vegetation sensitivity to orbital forcing and to a $p\mathrm{CO_2}$ halving using the IPSL-CM5A2 earth system model and the ORCHIDEE dynamic vegetation land surface model (see Materials and Methods). We first compare a set of seven late Eocene simulations [1120 parts per million (ppm), no ice sheet] describing extreme combinations of obliquity, precession, and eccentricity (Table 1). Although these configurations represent orbital end-members that were not attained (but regularly approached) during the studied 40-Ma to 32-Ma interval (fig. S1), they maximize the impact of each orbital configuration on the simulated global climate and vegetation and allow us to disentangle the role played by each parameter. In a second step, we compare this set of late Eocene simulations to a set of three early Oligocene simulations, with a $p\mathrm{CO_2}$ reduced to 560 ppm, an Antarctic ice sheet, and three different orbital configurations. Results are analyzed and compared to two available biome compilations from the latest Eocene and earliest Oligocene, respectively (*20*).

RESULTS

We first provide an overview of the climate and vegetation sensitivity to orbital forcing with late Eocene conditions. Then, we describe the impact of each orbital parameter on ITCZ, mid-latitude and high-latitude regions in that period, illustrated by detailed case studies. Last, we describe how orbital parameters affect the Oligocene climate and vegetation and replace our results in the broader context of faunal and floral shift at the greenhouse-icehouse transition. Note that the vegetation outputs of the land surface ORCHIDEE model are plant functional type (PFT) abundances (see Materials and Methods), which are used for detailed fine-resolution analysis of the paleovegetation evolution at a regional scale. In addition, PFTs were translated into biomes to be comparable to existing proxy compilations (*20*) and to identify global trends (see Materials and Methods).

Late Eocene global climatic and vegetation sensitivity to orbital forcing

The Eocene group of simulations (1120 ppm) yields continental mean annual temperatures (MATs) ranging from 22.9° to 24.7°C depending on the orbital configuration (Table 1). The highest MAT is obtained with the highest obliquities [hot boreal summer high obliquity (HBHO), hot austral summer high obliquity (HAHO), high obliquity (HO)] due to increased heating of high latitudes.

Table 1. Simulation boundary conditions and global continental climatic results. Precession is expressed as the longitude of the perihelion. Hot austral summer configurations are at perihelion on the 21st of December, which is close to the present-day value (4th of January), whereas hot boreal summer configurations are at perihelion on the 21st of June. Global results given in the right panel are mean annual temperature (MAT), mean annual temperature range (MATR), mean annual precipitation (MAP), land surface albedo, and desert proportion averaged along the year over the emerged lands.

Boundary conditions					Global continental results				
Orbital configuration	Eccentricity	Precession	Obliquity	$p\mathrm{CO_2}$ (ppm)	MAT (°C)	MATR (°C)	MAP (mm/year)	Albedo (%)	Desert (%)
Modern (MOD)	0.016715	102.7	23.441	1120	23.7	6.8	1177	8.9	30.9
				560	18.1	10.7	1080	10.6	31.2
Hot boreal summer high obliquity (HBHO)	0.06	270	24.5	1120	24.7	13.7	1163	9.1	32.4
Hot austral summer high obliquity (HAHO)	0.06	90	24.5	1120	24.2	3.9	1210	8.5	29.9
High obliquity (HO)	0	-	24.5	1120	23.8	8.5	1205	8.9	30.2
Low obliquity (LO)	0	-	22.1	1120	22.9	7.5	1140	9.2	31
Hot boreal summer low obliquity (HBLO)	0.06	270	22.1	1120	23.5	12.4	1152	9.5	32.5
				560	18.7	16.1	1072	11.2	32.3
Hot austral summer low obliquity (HALO)	0.06	90	22.1	1120	23.1	3.3	1148	8.6	30.2
				560	17.9	6.7	1076	12.1	34

Configurations with a precession favoring hot boreal summers and cold boreal winters [HBHO and hot boreal summer low obliquity (HBLO)] trigger the most seasonal climates with average mean annual temperature ranges (MATRs) higher than 12°C, whereas other configurations yield MATRs between 3.3° and 8.5°C. On a global scale, the more seasonal climates are also correlated to higher desert proportions (>32% of land surface) and high values of continental surface albedo (>9%; Table 1). This translates to higher seasonality in precipitations, which will be illustrated in the following case studies. These global trends provide a first-order glance at orbitally triggered variations in temperature, precipitation, and seasonality, and their spatial repartition is further detailed in Fig. 1.

The reference Eocene simulation [modern (MOD) orbital configuration, 1120 ppm] displays MATs ranging from ~45°C in the tropics to ~0°C in Antarctica (Fig. 1A). The most extreme temperature seasonality is simulated in Antarctica, Canada, and eastern Siberia (MATRs of ~40° to 45°C), while the equatorial regions experience very low MATR (<2.5°C; Fig. 1C). Mean annual precipitations (MAPs) are abundant at low latitudes (>3000 mm/year), while the subtropics, especially in Asia, show extremely arid regions (<500 mm/year; Fig. 1E). Orbitally forced variability drives modest MAT variations up to ±2°C especially at high latitudes and in the subtropics (Fig. 1B) due to compensating effects between seasons. MATR variability is more notable, with orbitally induced changes of ±7°C, particularly in mid-latitude continental interiors such as North America, Asia, and Antarctica (Fig. 1D). Tropical precipitations also display important variability, with changes as high as ±70% of MAP, which is closely related to summer ITCZ latitudinal shifts (Fig. 1F).

The MOD Eocene simulation produces low-latitude tropical forests gradually transforming into drier and more open environments (shrubland, savanna/woodland, or desert) as latitude increases (Fig. 1G). While temperate mixed and coniferous forests dominate from mid-latitudes poleward, the presence of warm-temperate forests remains substantial, especially in coastal environments (Australia, western Europe, and Patagonia). Continental Antarctica is the only region displaying cold forest biome. The evaluation of the vegetation sensitivity to orbital forcing (see Materials and Methods for details on the definition of this metric) highlights broad regions where the vegetation remains stable under changing orbital conditions (Fig. 1H, light gray shading). Stable tropical forests are mainly situated over the equator, while a variety of resilient warm, temperate, and cold forests are found at higher latitudes (their specific PFT composition is detailed in fig. S2). Conversely, many regions appear to be highly sensitive to orbital changes (Fig. 1H, dark gray shading), especially in the subtropics and poleward of 70°.

As a first validation, we compare our simulated biomes to a Priabonian (38 Ma to 33.9 Ma) biome reconstruction based on palynological data [symbols in Fig. 1H; (*20*)]. Biomes simulated in MOD Eocene match with ~54% of the proxy-based reconstruction. However, inclusion of the biome variability obtained with the six orbital end-member simulations increases the match to ~83%. Approximately 31% of the compilation sites exhibit a match between the data and the model in all simulations (squares in Fig. 1H), and ~52% in at least one of the orbital simulations (circles in Fig. 1H). On the contrary, the simulations fail to match the biome reconstruction in ~16% of the sites, suggesting that other sources than orbital forcing exist for these discrepancies. These sources may be manifold and are examined in Discussion. In the following sections, we focus on the regions showing the most important vegetation sensitivity to orbital forcing (boxes in Fig. 1H) and detail the climatic drivers behind these changes. The detailed biome distribution for each end-member simulation is given in fig. S3.

Low latitudes and the precession-driven ITCZ position

At low latitudes, the warm conditions experienced throughout the year in all orbital configurations only permit tropical trees or grasses to establish (Fig. 1). Therefore, precipitation is thought to be the main driver of vegetation changes observed in these regions (Fig. 1, F and H). This translates into highly variable proportions of bare soil relative to tropical vegetation or grasses, as exemplified through four sites (Fig. 2A, captions 1 to 4). They all present increasing proportions of vegetation in response to increasing summer insolation (Fig. 2C): Northeastern Brazil and Tanzania sites range from open and grassy tropical environments (in hot boreal configurations) to closed tropical forest (in hot austral configurations), while Mexico and southeastern China vary from woodland or shrubland environment (in hot austral settings) to open tropical forest environment (in hot boreal configurations). These biome variations appear to be tightly linked to the strength and duration of the summer precipitation peak (shown in ombrothermic diagrams in Fig. 2B), which is driven at these latitudes by the ITCZ seasonal migration (Fig. 1F). While the occurrence of open environments adapted to seasonally dry climate in these regions is attested in Asia, this type of vegetation is less firmly supported on other continents. The presence of woodland is suggested in Tanzania in the late-middle Eocene (*33*, *34*), as well as the increase for open dry-adapted habitat in the southern United States (*35*) and the possible early onset of the "dry diagonal" separating the Amazonian from the Atlantic forest biotas across Brazil (*31*, *36*).

The latitudinal position of the ITCZ, together with the extent of monsoonal conditions onshore, is strongly influenced by summer insolation (*37*). Therefore, orbital configurations leading to high summer insolation values are expected to produce latitudinal shifts in the subtropical summer rainfall regimes (Fig. 1F). The most spectacular ITCZ migrations are simulated over eastern Asia (from ~8°N to ~30°N), Central America (from ~18°N to ~23°N), and South America (from ~20°S to ~26°S) and drive a variability in the annual water budget in the subtropics that can be as high as 50 to 80% (Fig. 1F). Our simulations suggest that monsoon-like precipitation seasonality might have existed intermittently during astronomical extrema in the late Eocene, resulting in sporadic increases in moisture and more vegetated subtropical regions. While this pattern appears, at first order, mainly controlled by precession cyclicity, we also note that the "high obliquity" configurations tend to favor this enhanced inland ITCZ migration when compared to their "low obliquity" counterparts. However, obliquity does not trigger major insolation changes at these latitudes (<10 W/m^2 between HBHO and HBLO, while there is a difference of 115 W/m^2 between HBHO and HAHO). This suggests that summer insolation gradients involving higher latitudes ought to be considered to understand the full complexity of the process (see Discussion).

Mid-latitudes: Large-scale patterns and temperature thresholds

Between 25° and 50° (Fig. 1H), the vegetation response to orbital forcing is more complex due to an overlapping influence of temperature and precipitation change. The MATR at these latitudes is

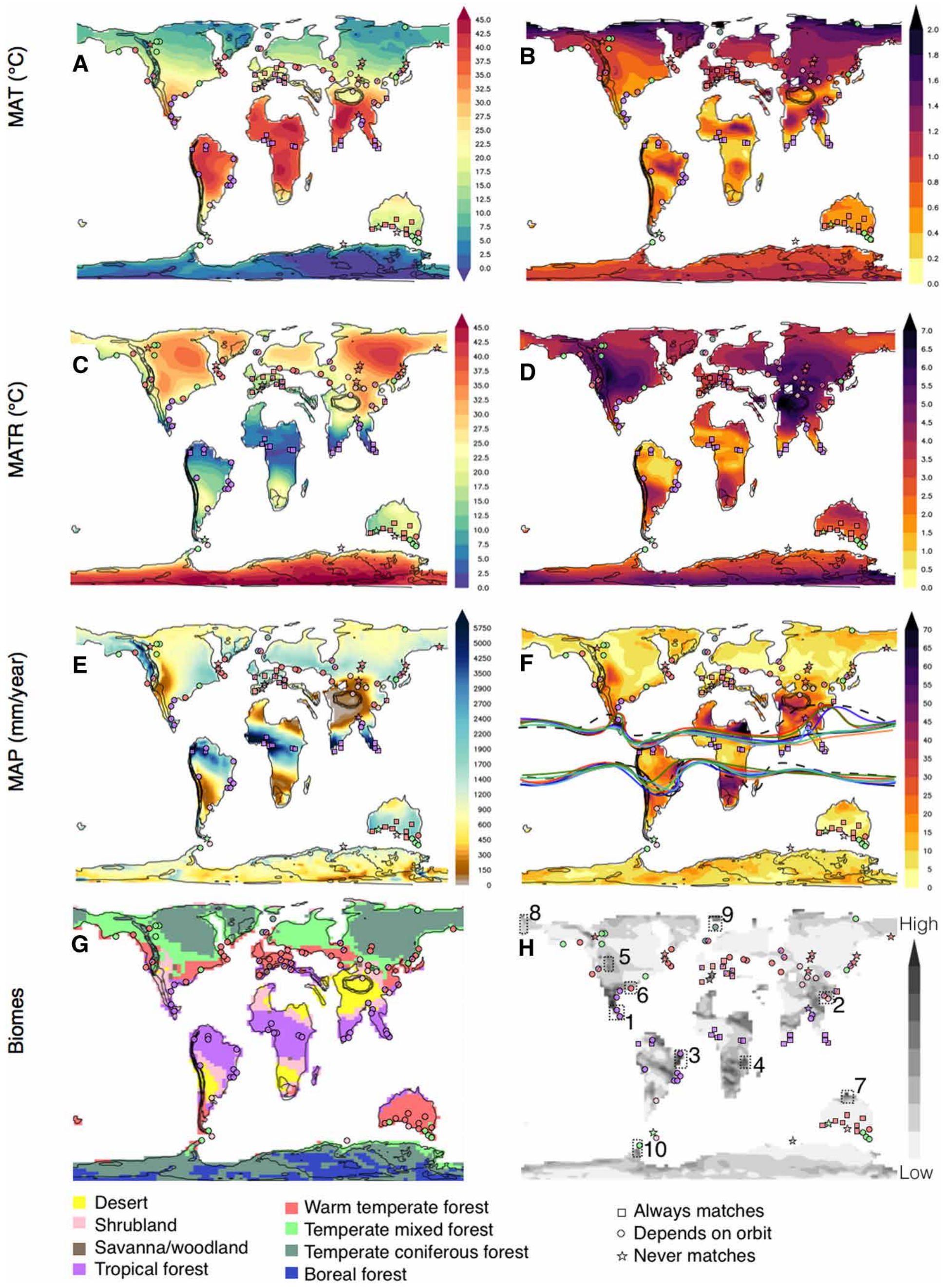

Fig. 1. Climate and vegetation variability under different orbital forcing for the Eocene (1120 ppm) orbital simulation set. (**A**, **C**, **E**, and **G**) Results obtained for the reference Eocene simulation using modern orbital parameters (MOD): mean annual temperature (MAT) (A), mean annual temperature range (MATR) (C), mean annual precipitation (MAP) (E), and biomes (G). (**B**, **D**, **F**, and **H**) Standard deviations (SDs) calculated for the same variables considering the seven 1120-ppm orbital simulations. SDs have the same unit as their corresponding variable except for the MAP (expressed in % of variation compared to the average MAP) and the biome variability, which is unitless. The biome variability in (H) is the cumulative SD of each PFT abundance normalized by the average number of PFTs defined in the grid cell and should be viewed as a low (white) to high (black) biome variability plot. In (H), numbered boxes highlight regions of extreme biome sensitivity to orbital forcing that is expanded upon in the following figures. Symbols overlain correspond to the biomes reconstructed (colors) for the Priabonian by the Pound and Salzmann compilation (*20*) and the degree of agreement with the biomes simulated by our Eocene simulation panel (symbols). In (F), colored lines represent the position of the ITCZ for each of the seven orbital configurations tested: MOD (full black), HBHO (red), HAHO (orange), HO (dark blue), LO (light blue), HALO (light green), HBLO (dark green), and present-day ITCZ position for comparison (dotted black).

consequent (from 10°C in coastal settings to 30°C in continental ones; Fig. 1C) and exhibits important variations (5° to 8°C) under varying orbital forcing (Fig. 1D). These temperature changes can induce the crossing of several PFT bioclimatic thresholds, particularly between tropical and temperate PFTs (table S1). In addition, MAPs can locally vary by up to 25% (Fig. 1F). Therefore, the simulated PFT variability is manifold: vegetation proportion versus desert, changes in each PFT relative abundance, or even (dis)appearance of PFT.

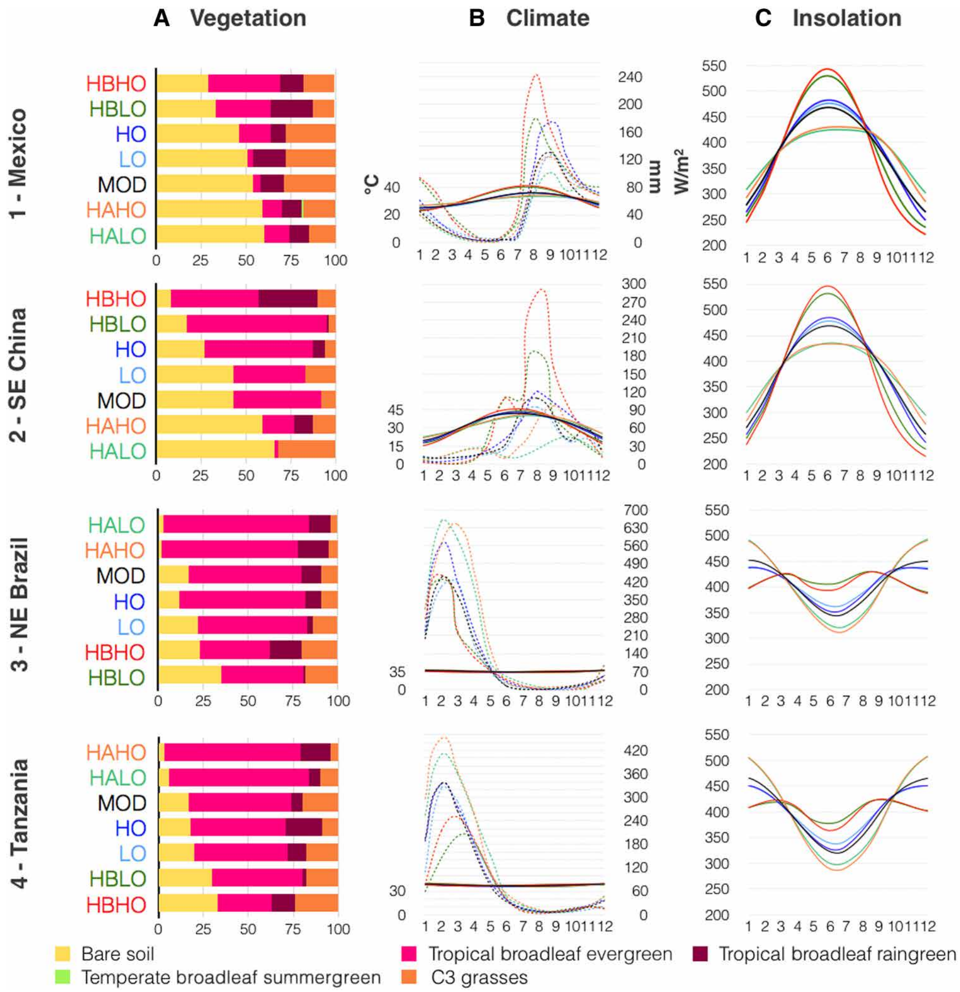

Fig. 2. Low-latitude zones of high biome variability illustrated through four representative sites: Mexico, southeastern China, northeastern Brazil, and Tanzania. (**A**) Vegetation: PFT composition (in %), each line corresponding to one of the seven orbital configurations described in Table 1. (**B**) Climate: Ombrothermic diagram displaying (for each orbital configuration) the evolution of temperature (full lines, in °C) and precipitation (dotted lines, in mm/month) along the year (horizontal axis). (**C**) Insolation profiles (in W/m^2) along the year. The orbital configurations' color coding is the same in all subpanels and in the following figures. Please note that the order of the simulation labels varies between sites in the northern and southern hemispheres according to decreasing summer insolation values.

Around 30°N, the PFT variability in coastal regions experiencing relatively high precipitation regimes (MAP > 1000 mm/year; Fig. 1, E and F) is generally dominated by temperature changes. This is exemplified by the "Louisiana" site (Fig. 3), displaying temperate-dominated PFT assemblages in hot boreal summer configurations (HBHO and HBLO) and gradually switching to tropical-dominated in hot austral summer configurations [hot austral summer low obliquity (HALO) and HAHO]. In these regions, the abundance of temperate trees appears to be well constrained by variations in the cold month mean temperature: Hot austral configurations generate warmer winters (~15°C; Fig. 3B) that tend to inhibit the settlement of temperate trees due to their bioclimatic limitations (cold month mean temperature$_{max}$ = 15.5°C for temperate broadleaf evergreen and temperate broadleaf summergreen PFTs; table S1). HBHO and HBLO configurations, on the other hand, trigger colder winters (cold month mean temperature < 15°C) that allow more competitive temperate trees to settle. Here again, the transition is mainly tuned to precession variations, as varying obliquity configurations [HO and low obliquity (LO)] does not seem to greatly affect these PFT proportions.

At higher latitudes (>40°), some sites experience noticeable biome variations. This is exemplified in the Montana area, where biomes as diverse as open mixed temperate forest (Fig. 3A, HALO configuration) shift to shrubland and woodland in the other configurations. This seems to corroborate observations from previous studies on paleosols, suggesting a possible orbital cyclicity in the MAP of this region, oscillating between ~400 and ~700 mm/year (*14*). Our findings simulate arid to subarid climatic conditions and demonstrate a strong response of the regional hydrology to precession, which could have affected pedogenic carbonate formation. Similarly, northern Australian biomes vary from tropical forest (more or less open forest, depending on the configurations) to woodland biomes (HBLO and HBHO configurations; Fig. 3A). The respective proportions of temperate versus tropical PFTs in these regions are easily attributed to insolation-driven winter temperature changes. In northern Australia, an increase in the proportion

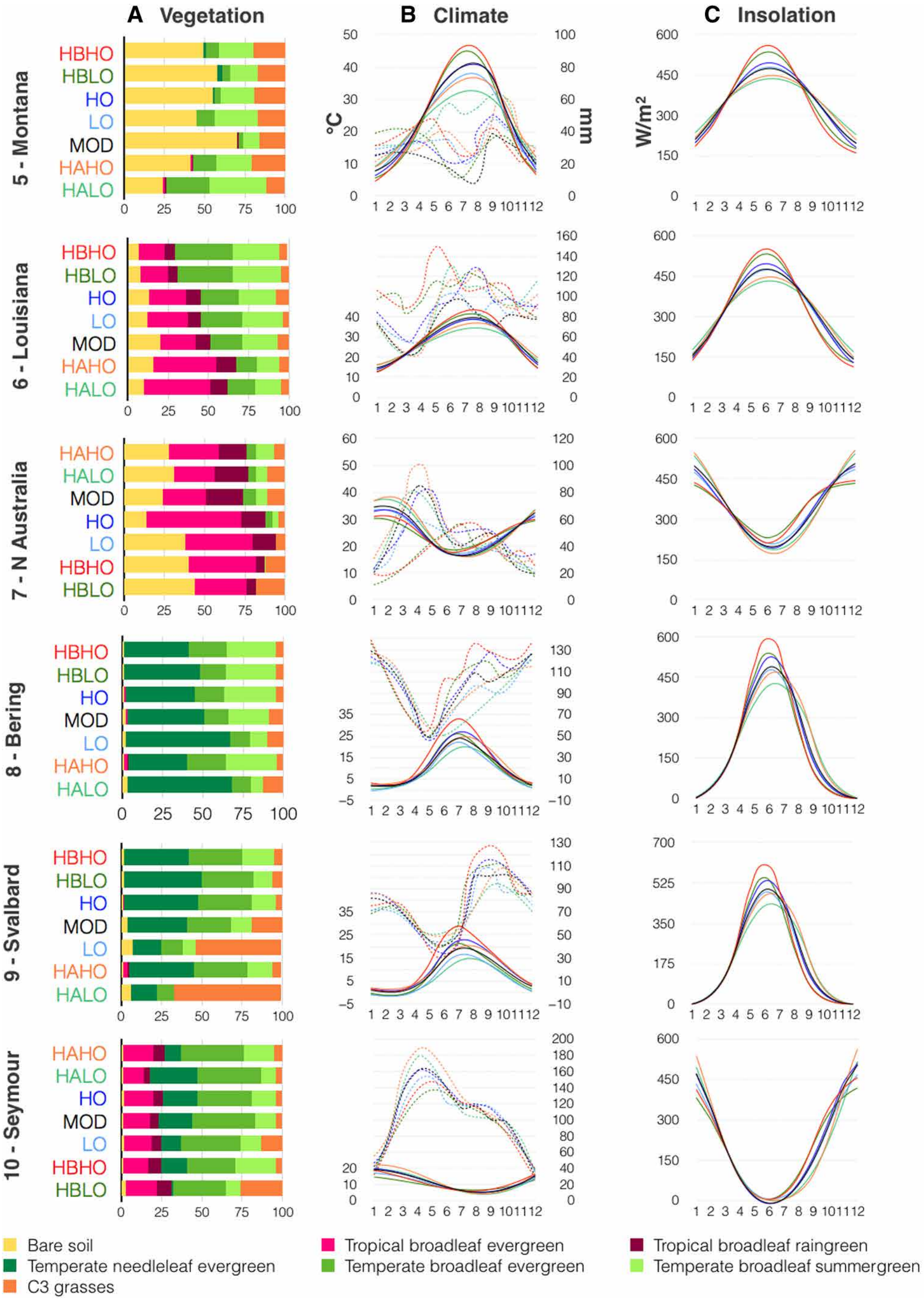

Fig. 3. Mid- and high-latitude zones of high biome variability illustrated through six representative sites: Montana, Louisiana, northern Australia, the Bering Strait, Svalbard, and Seymour Island. (**A** to **C**) The formalism is the same as in Fig. 2.

of temperate PFTs (up to 20%) is visible in configurations yielding colder winters (~17°C from July to September in HALO, HAHO, and HO). To a lesser extent, in Montana, warmer winter temperature (~10°C) triggered by hot austral configurations (HAHO and HALO) allows (rare) tropical trees to remain (~2%), while colder winters (~4°C) triggered by hot boreal configurations (HBHO and HBLO) allow (rare) conifers to settle (~2%).

The precipitation variations in these mid-latitude regions (up to 30% in MAP changes in Montana and 20% over northern Australia; Fig. 1B) are less straightforward to interpret than for the lower latitudes. Each site displays a specific signature that is dependent on its geographic environment. The biome diversity observed in Montana appears, for instance, to reflect the sensitivity of the region to the Jet Stream position (fig. S4). In detail, most configurations lead to important temperature gradients that produce a strongly "wavy" Jet Stream, which deviates Pacific westerlies toward higher latitudes and ultimately generates heavy summer precipitations over the American eastern coast and a depletion in rainfall over the Montana region (fig. S4A). On the contrary, the HALO experiment yields the coolest summer temperatures over northern America, which produces a more zonal Jet Stream (fig. S4B) and allows the input of more abundant summer precipitation from the Pacific.

High latitudes: Where obliquity is modulated by precession

Mid to high latitudes (~45°N to 70°N) are dominated by cool MATs (from 15° to 5°C in the Northern Hemisphere, down to 0°C in Antarctica; Fig. 1A), high MATR (mostly >25°C; Fig. 1C), and relatively low precipitations (MAP < 1000 mm/year; Fig. 1E). These climatic features translate into temperate mixed and temperate coniferous forests in the Northern Hemisphere, with some warm-temperate forest fringing Atlantic and Pacific coastal areas (e.g., west United States and Europe; figs. S2 and S3), and occasionally patches of more open shrubland zones at the highest latitudes. In the Southern Hemisphere, the vegetation is similarly characterized by temperate mixed and temperate coniferous forests with variable extension of cold forest in continental Antarctica (fig. S3). High latitudes host the widest regions of low PFT sensitivity to orbital forcing, for example, in Siberia, Canada, Australia, or Scandinavia (gray shading in Fig. 1H and detailed PFT compositions given in fig. S2). However, important biome changes exist locally, such as in the Bering, Svalbard, or the Seymour Island regions (Fig. 3).

At these latitudes, the main astronomical driver of climate and biome changes is obliquity through important summer insolation variations (Fig. 3). These variations translate into the most substantial MAT changes (up to 2°C; Fig. 1B), as well as MATR shifts (3° to 7°C; Fig. 1D) and MAP variations of 5 to 20% (Fig. 1F). The imprint of obliquity is particularly clear in Northern Hemisphere sites, where low obliquity configurations (LO and HALO) trigger the coldest and driest conditions (Fig. 3B), which favor either conifers (+20% from HO to LO and +30% from HAHO and HALO in Bering Strait) or grasses (+50% from HO to LO and +60% from HAHO and HALO in Svalbard). The fact that no temperature threshold modulates grass development in the model suggests that this expansion of grassland in low obliquity configurations is triggered by the slightly drier conditions in Svalbard. The Southern Hemisphere response is similar, although less contrasted, probably due to the oceanic climatic buffering effect. For instance, at Seymour Island, low obliquity settings favor conifers in HA configuration (+20% from HAHO to HALO) and grasses in other configurations (+8% from HO to LO and +20% from HBHO to HBLO). The simulations also suggest a precession-driven modulation of the obliquity forcing at high latitudes; the combination of low obliquity and precession yielding hot boreal (austral) summer in the Northern (Southern) Hemisphere does not trigger as many changes as that of low obliquity and other precessions (e.g., +7% conifers between HBLO and HBHO in Northern Hemisphere sites against +30% between HALO and HAHO).

Into the Oligocene: A paradigm change

To place the previous results in the context of declining $p\mathrm{CO}_2$ at the EOT, we performed an early Oligocene simulation, which is strictly comparable to the late Eocene reference simulation (MOD orbital configurations, same paleogeography), at the exception of the prescribed halving of the atmospheric CO_2 concentration (to 560 ppm) and the presence of an Antarctic ice sheet. As for the Eocene, we explore the sensitivity of the early Oligocene vegetation to orbital forcing, although in a simpler way. We conducted two orbital sensitivity experiments using the HALO and HBLO configurations that were approached in the early Oligocene at ~32 Ma (fig. S1). The global metrics calculated for the Oligocene (Table 1, 560-ppm simulations) indicate a ~5°C cooler world that is also drier (by about 100 mm/year), more seasonal (MATRs of 6.7° to 16.1°C), and with greater desert extent (31.2 to 34%). The largest changes in simulated biomes between the Eocene and Oligocene reference (MOD) simulations occur at mid to high latitudes (Fig. 4A), where the lower $p\mathrm{CO}_2$ levels induce the strongest temperature anomalies (4° to 13°C drop in MAT fig. S5A). In these areas, the cooler temperatures

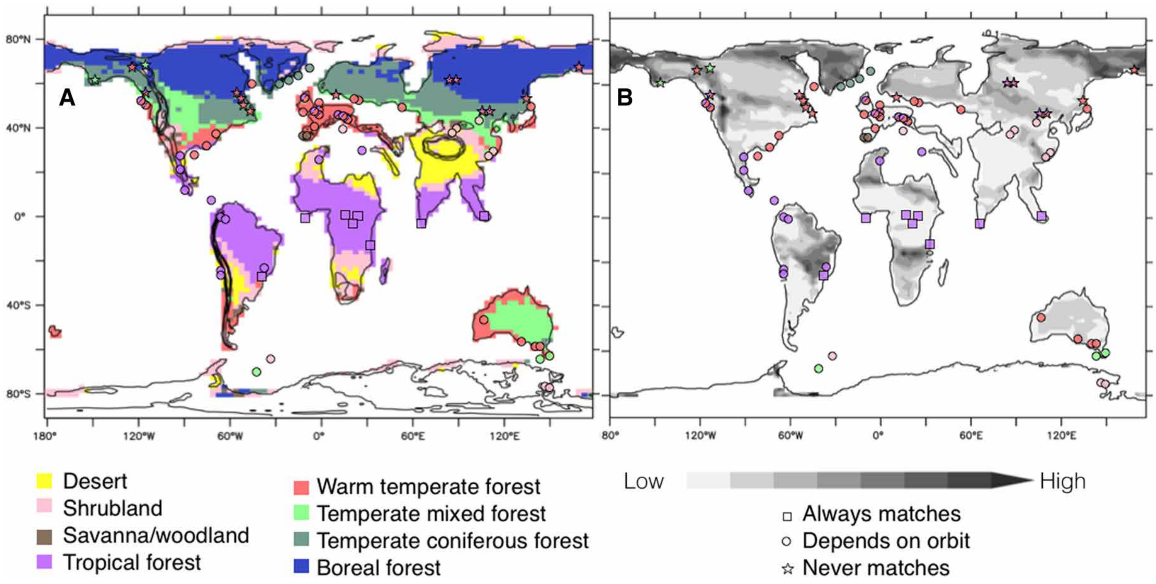

Fig. 4. Oligocene (560 ppm) vegetation variability under different orbital forcing. (**A**) Oligocene biome distribution simulated with modern orbital parameters and (**B**) cumulative PFT SDs obtained with the set of three simulations testing MOD, HALO, and HBLO configurations. Symbols in (A) and (B) correspond to a synthesized version (see Materials and Methods) of the Pound and Salzmann Rupelian biome compilation (*20*). The reader is referred to biomes and symbol legends of Fig. 1

narrow the tropical zone and shift all climatic envelopes toward lower latitudes, resulting in the equatorward migration of most biomes. This effect is particularly clear in Australia and eastern Asia, where the biome composition shifts mostly from warm-temperate forests in the Eocene toward temperate mixed forests. Scandinavia, Siberia, and Northern America biomes shift from temperate mixed forest to temperate coniferous or cold forests. Moreover, the global drying simulated for the early Oligocene, especially at mid to high latitudes (−30 to −100% in MAP poleward of 50° of latitude; fig. S5B), triggers increased proportions of woodland, savanna, and shrubland in Patagonia, Siberia, northern America, and Greenland.

The comparison with the early Oligocene biome compilation of (*20*) yields similarly good results for low-latitude and subtropical regions, with a good fit for tropical, shrubby, and warm-temperate environments (Fig. 4B). At these low latitudes, the model does not simulate important changes in the different biome locations between the ensemble of Eocene and Oligocene experiments, which seems coherent with the abundance of low-latitude sites displaying no clear change over the greenhouse-icehouse transition (*19*, *20*). A notable difference is the increased proportion of orbitally sensitive proxy sites (~70% of total sites for the early Oligocene compilation against 50% for the late Eocene; indicated by circles in Fig. 4B). This suggests that biomes became increasingly responsive to orbital forcing, especially at mid to high latitudes, in response to late Eocene/early Oligocene global climate cooling. The simulated increase in orbital sensitivity is related to the fact that PFTs are mainly constrained by the temperatures of the coldest months (table S1): In all our 1120-ppm simulations, winter temperatures generally remain above freezing regardless of the orbital configuration, whereas the 560-ppm simulations generate a wider range of cold temperatures, which enables a higher variety of biomes to settle (fig. S6). At northern high latitudes, several sites in eastern Greenland reflect the spreading of coniferous forests from the middle-late Eocene to the early Oligocene (*38*). This is coherent with the temperate coniferous to cold forest biomes simulated for the Oligocene (fig. S6). However, many proxy sites from the Pound and Salzmann compilation, especially in Siberia and eastern Canada, indicate notably warmer environments than the ones simulated with inferred biomes of temperate, warm-temperate, or even paratropical forests poleward of 60°N in continental settings. Most of these discrepancies (~20% of all the proxy sites, materialized as stars in Fig. 4B) are not resolved by either of the two other orbital settings tested, but other configurations may partially reduce the mismatch. For example, we have shown that HO conditions in the Eocene simulations yield more forested environments at high latitudes (Fig. 3). Moreover, it is probable that other forcings exert a crucial influence in these regions, some of which are detailed in the following section.

DISCUSSION

Paleoclimate "snapshot" representations: A reasonable approximation?

Given the difficulty to date pre-Quaternary fossils and sedimentological records with orbital precision, they are likely to be interpreted as representative of an "average climatic signature." In addition, most paleoclimate simulations designed to provide a physical background for these field interpretations use the present-day orbital configuration, mostly for comparison purposes with modern conditions, and also due to computing limitations. This simplistic approach may hold in regions displaying unaffected climatic envelopes under contrasted orbital forcing (e.g., fig. S2). However, in regions particularly sensitive to orbitally forced climate change, or in environments already close to a climate threshold (e.g., a cold month temperature boundary preventing tropical trees to settle), this methodology may generate important data-model comparison mismatch. For the late Eocene, some rare high-resolution deposits have demonstrated the strong impact orbital variation may have on regional hydrology and vegetation coverage (*12*, *14*). The handful of studies that have tested alternate orbital configurations for this same period have documented the potentially large climate response to this short-term forcing (*3*, *4*, *6*, *8*, *9*), but the implications in terms of vegetation coverage variability were not addressed, except for China in early Eocene conditions (*9*).

The present results provide sensitivity maps of plant community composition that can be used to aid in paleoenvironmental reconstructions, by describing possible biome distributions for the late Eocene and early Oligocene. These maps can serve as tools that highlight areas where particular care should be taken in the interpretation of long-term vegetation evolution, and related paleoenvironmental and paleoclimatic parameters. As shown in Results, the biome composition of 84% (resp. 80%) of late Eocene (resp. early Oligocene) proxy sites from the Pound and Salzmann pollen compilation is correctly simulated in at least one of the seven (resp. three) orbital simulations performed here. Our results suggest that apparently diverging pollen assemblages may be explained by orbital variability and that biome transitions may have occurred over short periods of time in some areas, which could have led to potentially diverging interpretations in terms of climate. Moreover, some paleoenvironments (e.g., semiarid versus more humid) were probably preferentially recorded at orbital time scale, depending on local water conditions and the morpho-anatomical characteristics of the plants (e.g., thin deciduous versus tough evergreen leaves) (*39*, *40*).

Case study: Comparison with high-resolution records in East Asia

Only one clear case study currently enables data-model comparison for orbital variability, highlighting the important need for additional high-resolution field work. The high dependence on precession of Northern Hemisphere summer precipitation in the tropics and subtropics (obliquity being a second-order factor at low latitudes) bears consistency with observations from the deep-lacustrine Jianghan Basin in eastern China (paleoposition: ~30°N, 110°E), which suggest eccentricity and precession-driven depositional patterns (*12*). Huang and Hinnov (*12*) propose that configurations inducing hot boreal summer, such as those approaching our HBHO and HBLO end-member cases, would have led to increased monsoon penetration inland and wetter summers, which would have favored silt and mudstone deposits. On the other hand, configurations inducing mild winters and cooler and drier summers, such as those approaching our HAHO and HALO end-member configurations, would have been more prone to evaporite deposits. Fossil pollen preserved in this basin indicates a relatively higher proportion of xerophytic taxa (*Ephedripites*) in the evaporite horizons, which corroborates this hypothesis (*12*).

Further inland, the shallow lacustrine Xining Basin (paleoposition: ~40°N, 100°E) also preserves alternations of orbitally paced mudstone and evaporitic deposits, although with a marked obliquity pattern identified during the 40-Ma to 34-Ma interval (*13*). The interpretation of Abels *et al.* (*13*) is different from the perennial lacustrine Jianghan deposits because, in shallow ephemeral lakes, the gypsum beds are correlated to relatively wetter phases and mudstones to drier ones within a globally semiarid context (*13*). This difference in orbital responses is interpreted to relate to the position of the Xining Basin, which is located within the scope of westerly moisture in a more continental setting and further away from the monsoon influence, and at higher latitudes, where the influence of obliquity tends to be stronger. The climate and vegetation reconstructed from the Xining Basin are, however, complex to interpret as they have also been shown to be tightly dependent on regional periodic regressions of the proto-Paratethys Sea in the west (*14*, *41*, *42*). This case study shows the potential of data-model comparison to provide physical constraints to proxy records focusing on the expression of orbital variability (*43*, *44*).

Intermittent monsoons: How often?

One of the most important outcomes of this study is the possible existence of orbitally induced intermittent monsoon-like climates as early as the late Eocene, primarily forced by precession (Fig. 2). It is well documented that precession configurations triggering warm boreal (austral) summer conditions amplify the Northern (Southern) Hemisphere monsoons via the amplification of continental summer low-pressure zones increasing the onshore deviation of the ITCZ (*37*, *43*). This feature appears to have been stable throughout the Cenozoic, as shown by modeling studies using Eocene boundary conditions (*3*, *7*, *8*), but also for the Miocene (*44*) and the present (*45*, *46*). A second-order forcing observed in our simulations is obliquity because an increased obliquity tends to enhance subtropical summer precipitations, particularly in Northern Hemisphere sites (Fig. 2). Many low-latitude proxies (e.g., speleothems and Mediterranean sapropels) also express a clear obliquity signal, although the effect of obliquity on incoming solar radiation at these latitudes is weak (in contrast to precession, which exerts a local forcing on ITCZ deviation through increased heating of low latitudes). The attempts to explain the low-latitude obliquity imprint in proxy records have often involved some remote teleconnections between low and high latitudes through ice volume variations (*43*), which is unlikely to be the main driver in our late Eocene ice-sheet free simulations. Another theory has emerged (*47*), however, showing that variations of the summer intertropical insolation gradient (SITIG; calculated between 23°N and 23°S) reflect both precession and obliquity variations without any need for ice-sheet variations. The mechanism involved is as follows: In HO configurations, the temperature gradient is low in the summer hemisphere and strong in the winter hemisphere due to increased cooling of the mid to high latitudes compared to the low latitudes. Therefore, HO configurations trigger stronger SITIG, which strengthens the winter Hadley cell branch and increases water vapor advection from the winter hemisphere toward the summer hemisphere tropics (*48*). The examination of the simulated SITIG in our experiments corroborates this mechanism, as our simulations producing the stronger SITIG (fig. S7) correspond to stronger summer precipitations in the four tropical sites highlighted in Fig. 2.

Comparing these simulated end-member SITIG values to the reconstructed SITIG variations along the 42-Ma to 34-Ma studied period [calculated from Laskar *et al.* (*49*), shown in fig. S7] allows us to evaluate the likelihood of occurrence of such SITIG gradient values during the late Eocene (fig. S7). While some configurations triggered extreme SITIG values that were not matched during the studied period (HBHO and HALO for the boreal summer and HBHO and HBLO for the austral summer; fig. S7), other configurations triggering summer precipitation peaks (HBLO in China and HBLO and HO in Mexico) produce SITIG values that were met during at least 2 to 6% of the 42-Ma to 34-Ma interval (fig. S7). Therefore, although this monsoon-like circulation might not represent the dominant climatic mode, it might have been a regularly occurring situation. As for the Southern Hemisphere, tropical summer precipitations show less sensitivity to obliquity (Fig. 2) and the SITIG gradient needed to trigger the required rainy season appears to be more ubiquitous (for example, the HALO configuration triggering SITIG values that were met about 20% of the time).

Implications for faunal dispersal events and biome variability

The medium to high biome variability of several narrow continental corridors in both the late Eocene and the early Oligocene, such as the Beringia, Turgai, and Anatolian land bridges, may have important biogeographical implications. The presence of these terrestrial corridors is paramount for biodiversity diaspora, and while the presence of such bridges at the EOT is well established (*27*, *50*–*53*), we suggest that orbital forcings might have modulated faunal and/or floral dispersal from Asia to other continents.

To illustrate this, we compare the biomes obtained for two contrasted orbital configurations (HALO and HBLO) for the late Eocene (1120 ppm) and the early Oligocene (560 ppm; Fig. 5), respectively, in the Eurasian region. Two dispersal routes between Asia and western Europe are proposed in this region (*27*): Dispersal is thought to have existed through the Turgai corridor during the late Eocene and until the Oligocene (31 Ma) before shifting to the Anatolian route, more to the south (*27*). While our spatial resolution cannot fully render the complex paleogeography of intricated islands in this region, our results, however, suggest that, if western Europe remained stably covered by warm-temperate biomes across the Late Eocene and Early Oligocene, the Turgai and Anatolian regions display more orbitally driven variability in biome composition (Fig. 5). The Late Eocene HALO configuration allows the establishment of warm-temperate biomes across all the Turgai region, therefore creating a continuous biome corridor. On the contrary, the HBLO configuration leads to cooler temperate biomes because of colder winters and breaks the continuity of the

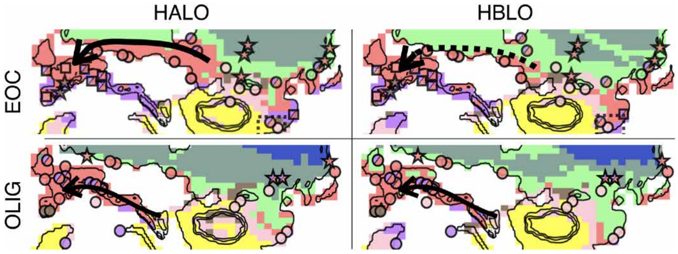

Fig. 5. Biome stability over the Eurasian Turgai and Anatolian land bridges. Evolution of the biomes simulated for the Eocene (1120 ppm, top row) and the Oligocene (560 ppm, bottom row) for two contrasted orbital settings (HALO and HBLO). The reader is referred to biomes and symbol legends of Fig. 1. Arrows show the main corridors of biome stability, which may have allowed faunal dispersal to occur: the northern dispersal route, through the Turgai land bridge, and the southern dispersal route, through the Anatolian emerged archipelagos, as described by Mennecart *et al.* (*27*).

warm-temperate biome despite an unchanged $p\mathrm{CO}_2$ (1120 ppm). This fragmentation of biomes along the corridor may have temporarily hampered faunal migrations occurring through this bridge in the late Eocene. In the early Oligocene cases, the Turgai route seems even more unlikely to act as dispersal corridor, given the notably cooler biomes simulated (temperate coniferous forest) contrasting strongly with the stable warm-temperate European forests. At lower latitudes, however, the Anatolian region presents a more homogeneous warm-temperate forest coverage, which is insensitive to orbital variations at 560 ppm. Therefore, while $p\mathrm{CO}_2$ appears to be the main driver of these widespread biome changes, our results suggest that orbital changes may have temporarily hampered faunal migrations via the Turgai route by fragmenting this biome corridor, especially during the late Eocene.

Limitations and future directions

A few points of systematic discordance between the data and the model remain (indicated by stars in Figs. 1H and 4B), accounting for 16% (20%) of the biome reconstructions for the late Eocene (early Oligocene). This mismatch might be explained by model limitations, such as the PFT parametrization, systematic biases, or a too coarse topography. For example, the position of "transition zones" between biomes is dependent on the PFT bioclimatic threshold parametrizations (presented in table S1) and biomization rules applied, which tend to rely on modern properties. In addition, the IPSL-CM5A2 model that was used here, despite various improvements on modern climatic features when compared to the IPSL-CM5A previous version, is known, as with its predecessor, to underestimate modern precipitation over South America and Asia (*54*, *55*), which likely applied in the Eocene as well (*56*).

In addition, besides general data uncertainties, such as biases of preservation, sample reworking, or imprecise dating or location, the use of fossil pollen and spores to generate biomes (*20*) also has limitations. For instance, palynological records can represent time-extensive accumulations of regional vegetation that may mask short-term temporal or spatial biome shifts. Although some pollen taxa present in the assemblages ("form genera," i.e., pollen that was not determined to species level) cannot be taken into account when generating paleo-biomes, use of a presence/absence matrix allows the representation of taxa regardless of their relative abundance (and evolution between the late Eocene and the early Oligocene). This can actually be viewed as a strength of the method, as it also compensates for other taphonomic constraints (e.g., interspecies differences in pollen production, dispersal, or preservation). While far less ubiquitous than palynomorphs, macrobotanical remains generally present a more local, shorter-term vegetation signal that can provide additional information (*57*). To make such a comparison at a global scale is, however, not currently possible, as high-resolution records across the EOT do not exist for all the biomes studied here.

The approach taken in this study could, in the future, be expanded in several directions, such as the use of the dynamic vegetation model online, instead of asynchronously (see Materials and Methods), to take into account vegetation feedback on all climatic components, especially the ocean (*58*). The use of orbital end-members allowed the exploration of the full range of orbital variability impact on biome composition, but more realistic orbital configurations could be used to test more precise hypotheses in specific regions. Moreover, the decrease in $p\mathrm{CO}_2$ and the inception of the Antarctic ice sheet are not the only important changes to be considered between the Eocene and Oligocene. Over the period of time considered here, additional paleogeographic changes could be introduced to perform a more realistic early Oligocene reconstruction, such as the important sea-level drop consecutive to the glaciation of Antarctica (*59*) that had major implications on continentality and possibly on atmospheric circulation (*60*). In Asia in particular, the sea-level drop enhanced the retreat of the Paratethys Sea, increased continentality, and deeply influenced the hydrology and temperatures, probably enhancing aridity in Central Asia (*61*, *62*) and reshaping the biodiversity in the region (*29*, *30*, *42*). Other paleogeographic features such as the Drake Passage deepening or the Tibetan Plateau uplift likely played a part in shaping the evolution of Cenozoic climate, but their precise evolution through time remains highly debated (*63*–*67*). Therefore, we believe that they should be the topic of dedicated modeling studies. Last, this work underlines the need for well-dated high-resolution proxy records in key areas combined with simulations constrained with more detailed paleogeography to better understand the role of orbital variability in climate records.

MATERIALS AND METHODS

IPSL-CM5A2 model components

IPSL-CM5A2 is an Earth system model designed for multimillennial simulations (*54*) composed of the atmospheric LMDz5A model, with a resolution of 3.75° × 1.89° (longitude × latitude) and 39 vertical layers from the surface up to 40 km high, the land surface ORCHIDEE model, and the ocean and sea ice NEMO–LIM2-PISCES model, in which the tripolar oceanic grid has a resolution varying between 0.5° and 2° and 31 vertical layers. The continuity of the processes at the interface between ocean and atmosphere is ensured by the OASIS coupler. The performances of the model and comparison with previously existing IPSL-CM5A model are fully described in a dedicated paper (*54*). The ORCHIDEE land surface model (*68*) is used in its three–soil layer (bucket) version, which includes river runoff and describes the vegetation through 13 PFTs, 2 anthropics (not used in this study), and 11 naturals (*69*): 8 forest PFTs, 1 bare soil PFT, and 2 grass PFTs (C_3 and C_4). As C_4 plants expanded starting from the late Miocene (*70*), this last PFT was deactivated. In the following modeling steps, the vegetation was either prescribed or allowed to evolve, as detailed below. In dynamic vegetation mode, starting from bare soil, all PFTs are able to grow, expand, or shrink, depending on the climatic conditions. In this configuration, each grid cell disposes of an infinite seed stock for each PFT, preventing the total and definitive extinction in case of a strongly unfavorable climatic episode during the experiment.

Simulation setup

Simulations are run in a two-step process: first, in atmosphere-ocean mode with an Eocene paleogeographic reconstruction (fig. S9A) and a forced vegetation map (fig. S9B) to produce realistic sea surface temperature (SST). At this step, a reference Eocene simulation (EOC_MOD) is performed using modern orbital parameters, a $p\mathrm{CO}_2$ at 1120 ppm (other greenhouse gas concentrations left to their preindustrial values), no ice sheets, and a solar constant reduced to 1360.19 W/m^2. This simulation was previously described and validated against late Eocene proxy sea surface and continental MAT compilations [see (*56*) and references therein]. After 3000 years, it reaches equilibrium (the deepest ocean layer shows a drift inferior to 0.1°C per century; fig. S8C). Six atmosphere-ocean simulations describing the end-members of eccentricity, obliquity, and precession (Table 1) are then performed restarting from the last day of the EOC_MOD experiment. These simulations run for 500 years, until reaching stable SST and oceanic heat content at 100 m depth (fig. S8D). Their SSTs are then averaged over the past 50 years of simulation and used to constrain the second phase of simulations, in which the PFT distribution of each orbital configuration is simulated using the atmosphere-vegetation mode. These dynamic vegetation simulations run for 150 years until reaching stable PFT composition. As some simulations displayed decadal variability in the climatic and vegetation fraction signals, the results are averaged over the last 50 years to grasp only the dominant PFT proportion signal. The early Oligocene simulation set follows the same sequence, the only differences being the reduced $p\text{CO}_2$ to 560 ppm and the presence of an Antarctic ice sheet.

Impact of the dynamic vegetation mode

The effect of prescribed versus dynamic vegetation is shown in fig. S9. In terms of vegetation coverage (as opposed to bare soil, hence regardless of the PFTs) (fig. S9A), the main changes are observed at the South Pole, as well as at the equator and the intertropical zone, where some areas present a 100% increase in vegetation coverage, meaning that regions that were seen as bare soil in the forced vegetation atmosphere-ocean simulation (EOC_MOD) actually grew a full vegetation coverage in dynamic vegetation mode (EOC_MOD_VD). This is observed in Antarctica, in Brazil, on the eastern coast of Asia, and in central Africa. This new vegetation repartition induces cooling up to 4°C in the Amazon region (fig. S9B), along with increased MAP by up to 30 to 100% (fig. S9, C and D) and latent heat flux increase of 20 to 50 W/m^2 in the areas that grew vegetation (fig. S9E). Previous studies demonstrated that major changes in land surface coverage (e.g., from a complete desert to a fully afforested land) could lead to significant retroactions on the oceanic component (*58*, *71*). The PFT changes observed between our two simulating steps remain, however, much more localized than these extreme sensitivity experiments. We nevertheless ran a test atmosphere-ocean simulation (MOD orbital configuration) forced with the PFT coverage map obtained with the MOD atmosphere-vegetation dynamical run and ensure PFT changes did not trigger major retroaction on the oceanic component.

Result treatment methodology

Each PFT coverage evolution is approximated through its summer fraction of vegetation to account for the maximal extent of the deciduous PFTs. The variability in PFT coverage (presented in Figs. 1H and 4B) between the seven different orbital experiments is then approximated, for each grid cell, through the sum of each PFT cover SD, normalized by the number of PFT defined on the grid cell averaged over the seven simulations. For comparison purposes to the Pound and Salzmann compilation, PFT coverage was subsequently treated to reflect biome distribution. We apply the methodology of (*72*), which considers simple bioclimatic thresholds and PFT dominance criteria that we adapted to the ORCHIDEE model (fig. S10) to define eight biomes: tropical forest, warm-temperate forest, temperate mixed forest, temperate to cool coniferous forest, cold forest, savanna, shrubs, and desert. The Pound and Salzmann compilations (*20*) are also simplified to match these biomes, as we cannot account for all the described environments (e.g., marshes or mangroves; table S2).

SUPPLEMENTARY MATERIALS

Supplementary material for this article is available at https://science.org/doi/10.1126/sciadv.abh2819

REFERENCES AND NOTES

1. T. Westerhold, N. Marwan, A. J. Drury, D. Liebrand, C. Agnini, E. Anagnostou, J. S. K. Barnet, S. M. Bohaty, D. De Vleeschouwer, F. Florindo, T. Frederichs, D. A. Hodell, A. E. Holbourn, D. Kroon, V. Lauretano, K. Littler, L. J. Lourens, M. Lyle, H. Pälike, U. Röhl, J. Tian, R. H. Wilkens, P. A. Wilson, J. C. Zachos, An astronomically dated record of Earth's climate and its predictability over the last 66 million years. *Science* **369**, 1383–1387 (2020).
2. D. J. Lunt, A. Ridgwell, A. Sluijs, J. Zachos, S. Hunter, A. Haywood, A model for orbital pacing of methane hydrate destabilization during the Palaeogene. *Nat. Geosci.* **4**, 775–778 (2011).
3. L. C. Sloan, C. Morrill, Orbital forcing and Eocene continental temperatures. *Palaeogeogr. Palaeoclimatol. Palaeoecol.* **144**, 21–35 (1998).
4. L. C. Sloan, M. Huber, Eocene oceanic responses to orbital forcing on precessional time scales. *Paleoceanography* **16**, 101–111 (2001).
5. P. J. Valdes, R. W. Glover, Modelling the climate response to orbital forcing. *Phil. Trans. R. Soc. A.* **357**, 1873–1890 (1999).
6. J.-B. Ladant, Y. Donnadieu, V. Lefebvre, C. Dumas, The respective role of atmospheric carbon dioxide and orbital parameters on ice sheet evolution at the Eocene-Oligocene transition. *Paleoceanography* **29**, 810–823 (2014).
7. J. S. Keery, P. B. Holden, N. R. Edwards, Sensitivity of the Eocene climate to CO2; and orbital variability. *Climate Past* **14**, 215–238 (2018).
8. A. Licht, M. van Cappelle, H. A. Abels, J.-B. Ladant, J. Trabucho-Alexandre, C. France-Lanord, Y. Donnadieu, J. Vandenberghe, T. Rigaudier, C. Lécuyer, D. Terry Jr., R. Adriaens, A. Boura, Z. Guo, A. N. Soe, J. Quade, G. Dupont-Nivet, J.-J. Jaeger, Asian monsoons in a late Eocene greenhouse world. *Nature* **513**, 501–506 (2014).
9. Z. Zhang, F. Flatøy, H. Wang, I. Bethke, M. Bentsen, Z. Guo, Early Eocene Asian climate dominated by desert and steppe with limited monsoons. *J. Asian Earth Sci.* **44**, 24–35 (2012).
10. R. M. DeConto, D. Pollard, P. A. Wilson, H. Pälike, C. H. Lear, M. Pagani, Thresholds for Cenozoic bipolar glaciation. *Nature* **455**, 652–656 (2008).
11. V. C. Thorn, R. DeConto, Antarctic climate at the Eocene/Oligocene boundary—Climate model sensitivity to high latitude vegetation type and comparisons with the palaeobotanical record. *Palaeogeogr. Palaeoclimatol. Palaeoecol.* **231**, 134–157 (2006).
12. C. Huang, L. Hinnov, Astronomically forced climate evolution in a saline lake record of the middle Eocene to Oligocene, Jianghan Basin, China. *Earth Planet. Sci. Lett.* **528**, 115846 (2019).
13. H. A. Abels, G. Dupont-Nivet, G. Xiao, R. Bosboom, W. Krijgsman, Step-wise change of Asian interior climate preceding the Eocene–Oligocene Transition (EOT). *Palaeogeogr. Palaeoclimatol. Palaeoecol.* **299**, 399–412 (2011).
14. N. Meijer, G. Dupont-Nivet, H. A. Abels, M. Y. Kaya, A. Licht, M. Xiao, Y. Zhang, P. Roperch, M. Poujol, Z. Lai, Z. Guo, Central Asian moisture modulated by proto-Paratethys Sea incursions since the early Eocene. *Earth Planet. Sci. Lett.* **510**, 73–84 (2019).
15. A. S. Gale, J. M. Huggett, H. PÄlike, E. Laurie, E. A. Hailwood, J. Hardenbol, Correlation of Eocene–Oligocene marine and continental records: Orbital cyclicity, magnetostratigraphy and sequence stratigraphy of the Solent Group, Isle of Wight, UK. *J. Geol. Soc. London* **163**, 401–415 (2006).
16. N. D. Sheldon, G. J. Retallack, Regional paleoprecipitation records from the Late Eocene and Oligocene of North America. *J. Geol.* **112**, 487–494 (2004).
17. A. Tosal, L. Valero, J. Sanjuan, C. Martín-Closas, Influence of short- and long-term climatic cycles on floristic change across the Eocene–Oligocene boundary in the Ebro Basin (Catalonia, Spain). *Comptes Rendus Palevol.* **18**, 925–947 (2019).
18. L. Valero, M. Garcés, L. Cabrera, E. Costa, A. Sáez, 20 Myr of eccentricity paced lacustrine cycles in the Cenozoic Ebro Basin. *Earth Planet. Sci. Lett.* **408**, 183–193 (2014).
19. D. K. Hutchinson, H. K. Coxall, D. J. Lunt, M. Steinthorsdottir, A. M. de Boer, M. Baatsen, A. von der Heydt, M. Huber, A. T. Kennedy-Asser, L. Kunzmann, J.-B. Ladant, C. H. Lear, K. Moraweck, P. N. Pearson, E. Piga, M. J. Pound, U. Salzmann, H. D. Scher, W. P. Sijp, K. K. Śliwińska, P. A. Wilson, Z. Zhang, The Eocene–Oligocene transition: A review of marine and terrestrial proxy data, models and model–data comparisons. *Climate Past* **17**, 269–315 (2021).
20. M. J. Pound, U. Salzmann, Heterogeneity in global vegetation and terrestrial climate change during the late Eocene to early Oligocene transition. *Sci. Rep.* **7**, 43386 (2017).
21. B. P. Kraatz, J. H. Geisler, Eocene–Oligocene transition in Central Asia and its effects on mammalian evolution. *Geology* **38**, 111–114 (2010).
22. J. Meng, M. C. McKenna, Faunal turnovers of Palaeogene mammals from the Mongolian Plateau. *Nature* **394**, 364–367 (1998).
23. J. Sun, X. Ni, S. Bi, W. Wu, J. Ye, J. Meng, B. F. Windley, Synchronous turnover of flora, fauna and climate at the Eocene–Oligocene Boundary in Asia. *Sci. Rep.* **4**, 7463 (2015).

24. J. Wasiljeff, A. Kaakinen, J. M. Salminen, Z. Zhang, Magnetostratigraphic constraints on the fossiliferous Ulantatal sequence in Inner Mongolia, China: Implications for Asian aridification and faunal turnover before the Eocene-Oligocene boundary. *Earth Planet. Sci. Lett.* **535**, 116125 (2020).
25. J. J. Hooker, M. E. Collinson, N. P. Sille, Eocene–Oligocene mammalian faunal turnover in the Hampshire Basin, UK: Calibration to the global time scale and the major cooling event. *J. Geol. Soc. London* **161**, 161–172 (2004).
26. S. C. Joomun, J. J. Hooker, M. E. Collinson, Changes in dental wear of *Plagiolophus minor* (Mammalia: Perissodactyla) across the Eocene–Oligocene transition. *J. Vertebr. Paleontol.* **30**, 563–576 (2010).
27. B. Mennecart, D. Geraads, N. Spassov, I. Zagorchev, Discovery of the oldest European ruminant in the late Eocene of Bulgaria: Did tectonics influence the diachronic development of the Grande Coupure? *Palaeogeogr. Palaeoclimatol. Palaeoecol.* **498**, 1–8 (2018).
28. E. Costa, M. Garcés, A. Sáez, L. Cabrera, M. López-Blanco, The age of the "Grande Coupure" mammal turnover: New constraints from the Eocene–Oligocene record of the Eastern Ebro Basin (NE Spain). *Palaeogeogr. Palaeoclimatol. Palaeoecol.* **301**, 97–107 (2011).
29. A. Favre, I. Michalak, C.-H. Chen, J.-C. Wang, J. S. Pringle, S. Matuszak, H. Sun, Y.-M. Yuan, L. Struwe, A. N. Muellner-Riehl, Out-of-Tibet: The spatio-temporal evolution of *Gentiana* (Gentianaceae). *J. Biogeogr.* **43**, 1967–1978 (2016).
30. A. Favre, M. Päckert, S. U. Pauls, S. C. Jähnig, D. Uhl, I. Michalak, A. N. Muellner-Riehl, The role of the uplift of the Qinghai-Tibetan Plateau for the evolution of Tibetan biotas. *Biol. Rev.* **90**, 236–253 (2015).
31. A. Fouquet, R. Recoder, M. Teixeira, J. Cassimiro, R. C. Amaro, A. Camacho, R. Damasceno, A. C. Carnaval, C. Moritz, M. T. Rodrigues, Molecular phylogeny and morphometric analyses reveal deep divergence between Amazonia and Atlantic Forest species of *Dendrophryniscus*. *Mol. Phylogenet. Evol.* **62**, 826–838 (2012).
32. J. V. Matthews, Tertiary land bridges and their climate: Backdrop for development of the present Canadian insect fauna. *Canadian Entomol.* **112**, 1089–1103 (1980).
33. B. F. Jacobs, Palaeobotanical studies from tropical Africa: Relevance to the evolution of forest, woodland and savannah biomes. *Phil. Trans. R. Soc. Lond. B* **359**, 1573–1583 (2004).
34. J. Saarinen, D. Mantzouka, J. Sakala, Aridity, cooling, open vegetation, and the evolution of plants and animals during the cenozoic, in *Nature Through Time*, E. Martinetto, E. Tschopp, R. A. Gastaldo, Eds. (Springer Textbooks in Earth Sciences, Geography and Environment, Springer International Publishing, 2020), pp. 83–107.
35. N. O. Frederiksen, Pulses of middle Eocene to earliest oligocene climatic deterioration in southern California and the Gulf Coast. *PALAIOS* **6**, 564–571 (1991).
36. V. A. Thode, I. Sanmartín, L. G. Lohmann, Contrasting patterns of diversification between Amazonian and Atlantic forest clades of Neotropical lianas (Amphilophium, Bignonieae) inferred from plastid genomic data. *Mol. Phylogenet. Evol.* **133**, 92–106 (2019).
37. T. M. Merlis, T. Schneider, S. Bordoni, I. Eisenman, Hadley circulation response to orbital precession. Part II: Subtropical continent. *J. Climate* **26**, 754–771 (2013).
38. J. S. Eldrett, D. R. Greenwood, I. C. Harding, M. Huber, Increased seasonality through the Eocene to Oligocene transition in northern high latitudes. *Nature* **459**, 969–973 (2009).
39. A. K. Behrensmeyer, S. M. Kidwell, R. A. Gastaldo, Taphonomy and paleobiology. *Paleobiology* **26**, 103–147 (2000).
40. R. Gastaldo, Taphonomic considerations for plant evolutionary investigations. *Paleobotanist* , 211–223 (1992).
41. M. Y. Kaya, G. Dupont-Nivet, J. Proust, P. Roperch, L. Bougeois, N. Meijer, J. Frieling, C. Fioroni, S. Özkan Altıner, E. Vardar, N. Barbolini, M. Stoica, J. Aminov, M. Mamtimin, G. Zhaojie, Paleogene evolution and demise of the proto-Paratethys Sea in Central Asia (Tarim and Tajik basins): Role of intensified tectonic activity at ca. 41 Ma. *Basin Res.* **31**, 461–486 (2019).
42. N. Barbolini, A. Woutersen, G. Dupont-Nivet, D. Silvestro, D. Tardif, P. M. C. Coster, N. Meijer, C. Chang, H.-X. Zhang, A. Licht, C. Rydin, A. Koutsodendris, F. Han, A. Rohrmann, X.-J. Liu, Y. Zhang, Y. Donnadieu, F. Fluteau, J.-B. Ladant, G. Le Hir, C. Hoorn, Cenozoic evolution of the steppe-desert biome in Central Asia. *Sci. Adv.* **6**, eabb8227 (2020).
43. A. C. Clement, A. Hall, A. J. Broccoli, The importance of precessional signals in the tropical climate. *Climate Dynam.* **22**, 327–341 (2004).
44. Z. Zhang, G. Ramstein, M. Schuster, C. Li, C. Contoux, Q. Yan, Aridification of the Sahara desert caused by Tethys Sea shrinkage during the Late Miocene. *Nature* **513**, 401–404 (2014).
45. D. S. Battisti, Q. Ding, G. H. Roe, Coherent pan-Asian climatic and isotopic response to orbital forcing of tropical insolation. *J. Geophys. Res. Atmos.* **119**, 11997–12020 (2014).
46. E. Tuenter, S. L. Weber, F. J. Hilgen, L. J. Lourens, The response of the African summer monsoon to remote and local forcing due to precession and obliquity. *Global Planet. Change* **36**, 219–235 (2003).
47. J. H. C. Bosmans, F. J. Hilgen, E. Tuenter, L. J. Lourens, Obliquity forcing of low-latitude climate. *Clim. Past* **11**, 1335–1346 (2015).
48. D. F. Mantsis, B. R. Lintner, A. J. Broccoli, M. P. Erb, A. C. Clement, H.-S. Park, The response of large-scale circulation to obliquity-induced changes in meridional heating gradients. *J. Climate* **27**, 5504–5516 (2014).
49. J. Laskar, P. Robutel, F. Joutel, M. Gastineau, A. C. M. Correia, B. Levrard, A long-term numerical solution for the insolation quantities of the Earth. *Astron. Astrophys.* **428**, 261–285 (2004).
50. L. Brikiatis, The De Geer, Thulean and Beringia routes: Key concepts for understanding early Cenozoic biogeography. *J. Biogeogr.* **41**, 1036–1054 (2014).
51. M. A. Akhmetiev, N. I. Zaporozhets, Paleogene events in Central Eurasia: Their role in the flora and vegetation cover evolution, migration of phytochore boundaries, and climate changes. *Stratig. Geol. Correl.* **22**, 312–335 (2014).
52. O. Eldholm, J. Thiede, Cenozoic continental separation between Europe and Greenland. *Palaeogeogr. Palaeoclimatol. Palaeoecol.* **30**, 243–259 (1980).
53. J. Liu, T. Su, R. A. Spicer, H. Tang, W.-Y.-D. Deng, F.-X. Wu, G. Srivastava, T. Spicer, T. Van Do, T. Deng, Z.-K. Zhou, Biotic interchange through lowlands of Tibetan Plateau suture zones during Paleogene. *Palaeogeogr. Palaeoclimatol. Palaeoecol.* **524**, 33–40 (2019).
54. P. Sepulchre, A. Caubel, J.-B. Ladant, L. Bopp, O. Boucher, P. Braconnot, P. Brockmann, A. Cozic, Y. Donnadieu, J.-L. Dufresne, V. Estella-Perez, C. Ethé, F. Fluteau, M.-A. Foujols, G. Gastineau, J. Ghattas, D. Hauglustaine, F. Hourdin, M. Kageyama, M. Khodri, O. Marti, Y. Meurdesoif, J. Mignot, A.-C. Sarr, J. Servonnat, D. Swingedouw, S. Szopa, D. Tardif, IPSL-CM5A2—An Earth system model designed for multi-millennial climate simulations. *Geosci. Model Dev.* **13**, 3011–3053 (2020).
55. P. J. Valdes, E. Armstrong, M. P. S. Badger, C. D. Bradshaw, F. Bragg, M. Crucifix, T. Davies-Barnard, J. J. Day, A. Farnsworth, C. Gordon, P. O. Hopcroft, A. T. Kennedy, N. S. Lord, D. J. Lunt, A. Marzocchi, L. M. Parry, V. Pope, W. H. G. Roberts, E. J. Stone, G. J. L. Tourte, J. H. T. Williams, The BRIDGE HadCM3 family of climate models: HadCM3@Bristol v1.0. *Geosci. Model Dev.* **10**, 3715–3743 (2017).
56. D. Tardif, F. Fluteau, Y. Donnadieu, G. Le Hir, J.-B. Ladant, P. Sepulchre, A. Licht, F. Poblete, G. Dupont-Nivet, The origin of Asian monsoons: A modelling perspective. *Clim. Past* **16**, 847–865 (2020).
57. A. Traverse, *Paleopalynology* (Springer, 2008).
58. U. Port, M. Claussen, Transitivity of the climate–vegetation system in a warm climate. *Clim. Past.* **11**, 1563–1574 (2015).
59. K. G. Miller, J. V. Browning, W. J. Schmelz, R. E. Kopp, G. S. Mountain, J. D. Wright, Cenozoic sea-level and cryospheric evolution from deep-sea geochemical and continental margin records. *Sci. Adv.* **6**, eaaz1346 (2020).
60. F. Fluteau, G. Ramstein, J. Besse, Simulating the evolution of the Asian and African monsoons during the past 30 Myr using an atmospheric general circulation model. *J. Geophys. Res. Atmos.* **104**, 11995–12018 (1999).
61. R. E. Bosboom, G. Dupont-Nivet, A. J. P. Houben, H. Brinkhuis, G. Villa, O. Mandic, M. Stoica, W. J. Zachariasse, Z. Guo, C. Li, W. Krijgsman, Late Eocene sea retreat from the Tarim Basin (west China) and concomitant Asian paleoenvironmental change. *Palaeogeogr. Palaeoclimatol. Palaeoecol.* **299**, 385–398 (2011).
62. L. Bougeois, G. Dupont-Nivet, M. de Rafélis, J. C. Tindall, J.-N. Proust, G.-J. Reichart, L. J. de Nooijer, Z. Guo, C. Ormukov, Asian monsoons and aridification response to Paleogene sea retreat and Neogene westerly shielding indicated by seasonality in Paratethys oysters. *Earth Planet. Sci. Lett.* **485**, 99–110 (2018).
63. Y. Lagabrielle, Y. Goddéris, Y. Donnadieu, J. Malavieille, M. Suarez, The tectonic history of Drake Passage and its possible impacts on global climate. *Earth Planet. Sci. Lett.* **279**, 197–211 (2009).
64. A. Toumoulin, Y. Donnadieu, J. -B. Ladant, S. J. Batenburg, F. Poblete, G. Dupont-Nivet, Quantifying the effect of the Drake Passage opening on the Eocene ocean. *Paleoceanogr. Paleoclimatol.* **35**, e2020PA003889 (2020).
65. J.-B. Ladant, Y. Donnadieu, L. Bopp, C. H. Lear, P. A. Wilson, Meridional contrasts in productivity changes driven by the opening of drake passage. *Paleoceanogr. Paleoclimatol.* **33**, 302–317 (2018).
66. C. Wang, J. Dai, X. Zhao, Y. Li, S. A. Graham, D. He, B. Ran, J. Meng, Outward-growth of the Tibetan Plateau during the Cenozoic: A review. *Tectonophysics* **621**, 1–43 (2014).
67. R. Spicer, T. Su, P. J. Valdes, A. Farnsworth, F.-X. Wu, G. Shi, T. E. V. Spicer, Z. Zhou, Why 'the uplift of the Tibetan Plateau' is a myth? *Natl. Sci. Rev.* 19 (2020).
68. G. Krinner, N. Viovy, N. de Noblet-Ducoudré, J. Ogée, J. Polcher, P. Friedlingstein, P. Ciais, S. Sitch, I. C. Prentice, A dynamic global vegetation model for studies of the coupled atmosphere-biosphere system: DVGM FOR COUPLED CLIMATE STUDIES. *Global Biogeochem. Cycles* **19**, 10.1029/2003GB002199, (2005).
69. B. Poulter, P. Ciais, E. Hodson, H. Lischke, F. Maignan, S. Plummer, N. E. Zimmermann, Plant functional type mapping for earth system models. *Geosci. Model Dev.* **4**, 993–1010 (2011).
70. T. E. Cerling, Y. Wang, J. Quade, Expansion of C4 ecosystems as an indicator of global ecological change in the late Miocene. *Nature* **361**, 344–345 (1993).
71. U. Port, M. Claussen, V. Brovkin, Radiative forcing and feedback by forests in warm climates – a sensitivity study. *Earth Syst. Dynam.* **7**, 535–547 (2016).

72. A. Dallmeyer, M. Claussen, V. Brovkin, Harmonising plant functional type distributions for evaluating Earth system models. *Clim. Past* **15**, 335–366 (2019).

Acknowledgments: We thank C. Jaramillo for his critical reading of the first draft of the manuscript as well as the three anonymous reviewers for their insightful comments that helped improve the quality and the clarity of the paper. **Funding:** This work was granted access to the HPC resources of TGCC under the allocation 2018-A0050107601 and 2019-A0070107601 made by GENCI. This work was funded by the INSU-CNRS SYSTER. G.D.-N., A.T., and N.B. acknowledge support from ERC MAGIC grant 649081. Y.D. acknowledges support from ANR AMOR (ANR-16-CE31-0020). **Author contributions:** D.T., F.F., Y.D., J.-B.L., and G.L.H. designed and performed simulations. All the authors contributed to the results analysis and discussion. D.T. drafted the paper, and all authors contributed to the improvement of the final version, as well as answering the reviewers and modifying the manuscript accordingly. **Competing interests:** The authors declare that they have no competing interests. **Data and materials availability:** All data needed to evaluate the conclusions in the paper are present in the paper and/or the Supplementary Materials. LMDZ, XIOS, NEMO, and ORCHIDEE are released under the terms of the CeCILL license. OASIS MCT is released under the terms of the Lesser GNU General Public License (LGPL). IPSL-CM5A2 code is publicly available through svn with the following command lines: svn co http://forge.ipsl.jussieu.fr/igcmg/svn/modipsl/branches/publications/IPSLCM5A2.1_11192019 (last access: 20 April 2020, IPSL Climate Modelling Centre, 2020a) modipsl cd modipsl/util;./model IPSLCM5A2.1. The mod.def file provides information regarding the different revisions used, namely, NEMOGCMbranchnemo_v3_6_STABLErevision6665- XIOS2branchs/xios-2.5revision1763-IOIPSL/srcsvntags/v2_2_2- LMDZ5branches/IPSLCM5A2.1rev3591-branches/publications/ORCHIDEE_IPSLCM5A2.1.r5307rev6336- OASIS3-MCT2.0_branch(rev4775IPSLserver). The login/password combination requested at first use to download the ORCHIDEE component is anonymous/anonymous. We recommend referring to the project website http://forge.ipsl.jussieu.fr/igcmg_doc/wiki/Doc/Config/IPSLCM5A2 (last access: 20 April 2020, IPSL Climate Modelling Centre, 2020b) for a proper installation and compilation of the environment.

Submitted 1 March 2021
Accepted 3 September 2021
Published 22 October 2021
10.1126/sciadv.abh2819

Citation: D. Tardif, A. Toumoulin, F. Fluteau, Y. Donnadieu, G. Le Hir, N. Barbolini, A. Licht, J.-B. Ladant, P. Sepulchre, N. Viovy, C. Hoorn, G. Dupont-Nivet, Orbital variations as a major driver of climate and biome distribution during the greenhouse to icehouse transition. *Sci. Adv.* **7**, eabh2819 (2021).

Science Advances

Orbital variations as a major driver of climate and biome distribution during the greenhouse to icehouse transition

Delphine TardifAgathe ToumoulinFrédéric FluteauYannick DonnadieuGuillaume Le HirNatasha BarboliniAlexis LichtJean-Baptiste LadantPierre SepulchreNicolas ViovyCarina HoornGuillaume Dupont-Nivet

Sci. Adv., 7 (43), eabh2819.

Science Advances (ISSN) is published by the American Association for the Advancement of Science. 1200 New York Avenue NW, Washington, DC 20005. The title *Science Advances* is a registered trademark of AAAS.